nature communications

Article

https://doi.org/10.1038/s41467-025-62853-0

Non-reciprocal frequency conversion in a non-Hermitian multimode nonlinear system

Received: 17 October 2024

Accepted: 1 August 2025

Published online: 14 August 2025

Check for updates

Sahil Pontula[1,2,3] ✉, Sachin Vaidya[1,3], Charles Roques-Carmes[3,4], Shiekh Zia Uddin[1,3], Marin Soljačić[1,3] & Yannick Salamin[1,3,5] ✉

Nonlinear optics has become the workhorse for countless applications in classical and quantum optics, from optical bistability to single photon pair generation. However, the intrinsic weakness of optical nonlinearity and reciprocity of nonlinear interactions generally places stringent limits on the efficiency of nonlinear optical processes and their ability to be tailored for advanced applications in multimode systems. Here, motivated by recent advances in using non-Hermitian photonics and gain/loss engineering to enable non-reciprocal light transport, we explore how the interplay between non-Hermiticity and optical nonlinearity leads to a fundamentally new regime of nonlinear frequency conversion. We show how non-Hermitian coupling between discrete frequency modes can result in non-reciprocal flow of energy in a frequency dimension, closely resembling the non-Hermitian skin effect (NHSE). Applying our theory to a multimode nonlinear cavity supporting cascaded nonlinear processes, we demonstrate chiral energy flow in a frequency dimension, leading to long-range frequency shifts of quasi-continuous wave sources, shaped frequency combs robust to defects and disorder, terahertz (THz) generation far exceeding the Manley-Rowe limit, and nonlinear multimodal limit cycles for multi-frequency pump-probe spectroscopy.

Nonlinear optical systems have long been a cornerstone of advanced photonics, enabling a wide range of applications from frequency conversion[1,2] and high-speed communication[3] to quantum information processing[4,5]. More recently, the focus has shifted to multimode nonlinear systems, which offer the potential for more complex interactions through nonlinear processes. For instance, frequency combs, which consist of many discrete frequency modes, have found widespread application in precision metrology and high-capacity data transmission[6–8]. However, traditional nonlinear optical systems are constrained by the intrinsic optical properties of nonlinear materials, which are generally weak and obey laws of reciprocity. This restricts conversion efficiencies and the ability to manipulate nonlinear energy flow for more sophisticated functionalities. Achieving control over nonlinear interactions in multimode systems could enable breakthroughs such as overcoming the standard efficiency limits in frequency conversion[9–11] and realizing new topological phenomena in real and synthetic frequency dimensions[12–14]. Despite these promising applications, control over multimode nonlinear systems has been difficult to achieve, owing to high dimensionality and the intrinsic complexity of many nonlinear interactions.

The introduction of non-Hermitian elements into optical systems has opened new avenues for controlling light-matter interactions and energy flow in real and synthetic dimensions[15–21]. These systems can exhibit unique phenomena not seen in traditional Hermitian systems, such as exceptional points[22–24], non-reciprocity[22], parity-time ($\mathcal{PT}$) symmetry breaking[25], and the non-Hermitian skin effect (NHSE)[26–28]. Recent studies have shown that breaking reciprocity in a discrete synthetic frequency dimension can realize non-Hermitian Hamiltonians and topological windings in the photonic band structure[29,30]. However, the intersection of non-reciprocity in a frequency dimension

[1]Department of Physics, MIT, Cambridge, MA, USA. [2]Department of Electrical Engineering and Computer Science, MIT, Cambridge, MA, USA. [3]Research Laboratory of Electronics, MIT, Cambridge, MA, USA. [4]E. L. Ginzton Laboratories, Stanford University, Stanford, CA, USA. [5]CREOL, The College of Optics and Photonics, University of Central Florida, Orlando, Florida, USA. ✉e-mail: spontula@mit.edu; yannick.salamin@ucf.edu

and nonlinear frequency conversion has not been explored, although exciting related work in the optomechanical domain has recently been reported[31], in addition to reports of nonlinear skin modes and shaping of quantum noise in non-reciprocal Hatano-Nelson systems with on-site Kerr nonlinearity[32,33]. Overall, considerable attention has been given to breaking spatial reciprocity in optical and optomechanical systems[34–41], with a notable gap existing in the interplay between optical nonlinearity and non-reciprocal coupling in multimode nonlinear systems.

In this work, we investigate a multimode nonlinear cavity system that leverages both Hermitian and non-Hermitian interactions to achieve enhanced control over nonlinear energy flow. Our system features a cavity supporting multiple frequency modes that are nonlinearly coupled to a common idler mode. This configuration supports cascaded parametric upconversion and downconversion processes, forming a frequency comb. We demonstrate that the interplay between nonlinear Hermitian coupling, dissipation, and anti-Hermitian amplitude modulation can be utilized to shape nonlinear frequency conversion processes. By fine-tuning the balance between nonlinearity, dissipation, and amplitude modulation, we achieve non-reciprocal frequency conversion and enhanced energy localization in a chiral mode. This boosts the energy conversion efficiency for both the chiral mode as well as the idler mode orders of magnitude above efficiencies imposed by reciprocity. Our results further reveal how nonlinear frequency conversion can be controlled using system parameters to generate frequency combs of arbitrary asymmetry, with the asymmetry remaining robust to defects and disorder in the frequency comb. We also identify different behaviors (phases) in the nonlinear, non-Hermitian system's mean-field dynamics, demonstrating stable multimodal limit cycles that could provide a new resource for time-domain multiplexing and multi-frequency pump-probe spectroscopy[42].

Results

Theory and system description

The system under consideration is depicted in Fig. 1a, representing a *multimodal* nonlinear cavity that supports cascaded three-wave mixing processes mediated by a common idler bath mode at frequency ω_T. A pump mode at ω_0 initiates cascaded parametric upconversions and downconversions mediated by the common idler mode to create blueshifted and redshifted modes relative to the pump mode, forming a comb with spacing ω_T. Energy conservation for each three-wave mixing process reads $\omega_n = \omega_{n-1} - \omega_T$, where $\omega_{n>0}$ corresponds to the comb mode associated with the generation of n idler photons, so that $\omega_n = \omega_0 - n\omega_T$.

The system additionally undergoes amplitude modulation at frequency $\omega_{\mathrm{mod}} = \omega_T$, generating anti-Hermitian coupling between neighboring modes (we consider the case $\omega_{\mathrm{mod}} \ll \omega_T$ in the Supplementary Information). We assume here that the modulation is provided by an external drive that gives rise to a modulation index $J \ll 1$. However, amplitude modulation can also be self-started by the cascaded optical nonlinearity without an external drive at ω_{mod}, as shown in the Supplementary Information. When externally driven, ω_{mod} sets the idler frequency $\omega_T = \omega_{\mathrm{mod}}$ as long as the three-wave mixing process $\{\omega_0, \omega_1, \omega_T\}$ lies within the nonlinear crystal's phase matching bandwidth, since the system is not seeded[43]. When self-driven, the difference frequency $\omega_T = \omega_0 - \omega_1$ naturally sets the modulation frequency ω_{mod}. The composite Hamiltonian reads (see Methods)

$$\begin{aligned}\frac{\mathcal{H}}{\hbar} &= (\omega_T - i(\gamma_T + \mu_T))\hat{a}_T^\dagger \hat{a}_T + \sum_n (\omega_n - i(\gamma + \mu))\hat{a}_n^\dagger \hat{a}_n \\ &+ i\sum_n (\beta_{T,n,n-1}\hat{a}_T^\dagger + \kappa)\hat{a}_n^\dagger \hat{a}_{n-1} \\ &- i\sum_n (\beta_{T,n,n-1}^* \hat{a}_T - \kappa^*)\hat{a}_n \hat{a}_{n-1}^\dagger \\ &+ i\sqrt{2\gamma}s_0(\hat{a}_0^\dagger - \hat{a}_0).\end{aligned} \tag{1}$$

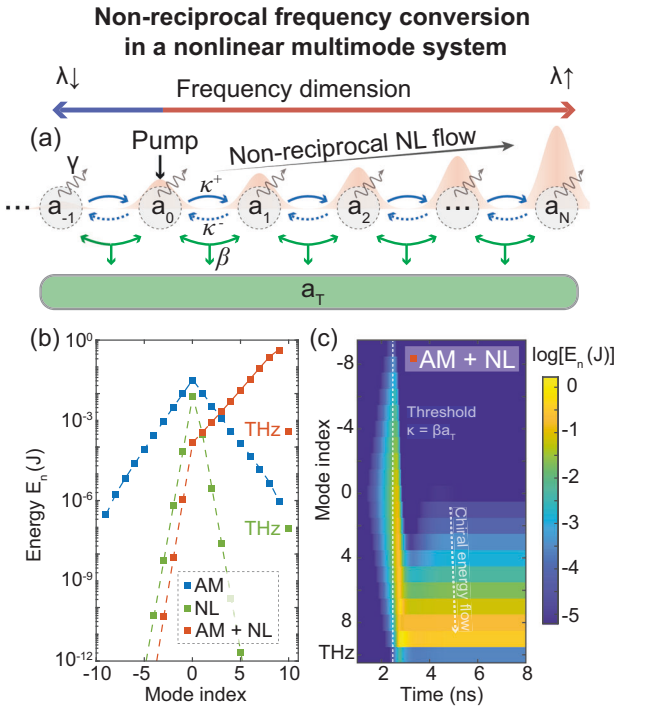

Fig. 1 | Shaping nonlinear energy flow in a non-Hermitian nonlinear multimode cavity. a Tight-binding schematic of nearest-neighbor couplings in a frequency multimode system with second-order nonlinearity. The interplay between nonlinear Hermitian coupling (NL) mediated by a common idler mode and the anti-Hermitian coupling generated by amplitude modulation (AM) at the idler frequency breaks reciprocity in the frequency conversion ($\kappa^+ \neq \kappa^-$), which can create unidirectional energy flow in the frequency dimension. **b** The presence of anti-Hermitian coupling through AM or Hermitian coupling through NL alone is insufficient to break symmetry in the frequency conversion process. However, the presence of both couplings simultaneously generates an effective non-Hermitian system that can bias frequency downconversions and create an asymmetric frequency comb. **c** In the nonlinear, non-Hermitian system, the interplay between NL and AM is reflected in the temporal dynamics of the modal amplitudes since the nonlinear coupling is time-dependent, $\beta a_T(t)$. The initial frequency conversion is symmetric since $\kappa^+ = -\kappa^-$ (purely AM coupling). As the idler mode is populated, $\beta a_T \to \kappa$. A threshold is reached where reciprocity in upconversion/downconversion is broken and an NHSE-type phenomenon in the frequency dimension occurs, with all energy flowing to the chiral mode a_N. In (**b**, **c**), $2N+1 = 19$, $\beta_0 = 2 \times 10^{-4}$ J$^{-1/2}$, $\kappa = 7.8 \times 10^9$ s^{-1}, $Q_0 = 9 \times 10^5$, $\mu = 0.1\gamma$, $Q_T = 10^3$, and $\hbar\omega_0|s_0|^2 = 5$ MW. In this system, the pump frequency $\omega_0 = 2\pi \cdot 282$ THz, and the idler frequency $\omega_T = 2\pi \cdot 1.06$ THz.

From this Hamiltonian, equations of motion for the mean field amplitudes of the comb modes a_n (with energy $E_n = \hbar\omega_n|a_n|^2$) and idler bath mode a_T (with energy $E_T = \hbar\omega_T|a_T|^2$) in the interaction picture read

$$\begin{aligned}\dot{a}_T &= \sum_n \beta_{T,n,n-1} a_n^* a_{n-1} - (\gamma_T + \mu_T)a_T \\ \dot{a}_n &= -(\beta_{T,n,n+1}^* a_T - \kappa^*)a_{n+1} + (\beta_{T,n,n-1} a_T^* + \kappa)a_{n-1} \\ &\quad - (\gamma + \mu)a_n + \sqrt{2\gamma}s_n\delta_{n,0},\end{aligned} \tag{2}$$

where $\beta_{T,n,n-1} = \beta_0\sqrt{\hbar\omega_T\omega_n\omega_{n-1}}$ is the nonlinear coupling strength with β_0 a constant dependent on the second-order nonlinearity (see Supplementary Information), κ the strength of amplitude modulation, s_n the strength of external pumping, and γ, μ the outcoupling and intrinsic losses. We provide numerical estimates for these physical parameters in the Supplementary Information. Although we simulate systems in the text with the full frequency dependence of $\beta_{T,n,n-1}$, because the comb span is generally much smaller than the frequency of an individual comb mode, we will approximate $\beta_{T,n,n-1} \to \beta$ as constant for simplicity in further

expressions. As we will show, the interplay between on-site non-Hermiticity (loss) and non-Hermitian intermodal coupling in this model will enable us to have a new degree of freedom in controlling nonlinear energy flow in a frequency dimension and shaping nonlinear frequency conversion. We note that, in the Hamiltonian description of this system, a unitary transformation can be used to move the off-diagonal non-Hermiticity in the frequency mode basis onto the diagonal (see Methods). Specifically, this shows how nonlinearity can play the role of gain/loss in the frequency dimension, which will be crucial for non-reciprocal frequency conversion.

The nonlinear system of differential equations specified by Eq. (2) can be numerically solved as a function of time starting from an initial condition where the fields are zero. If the system reaches steady state, the power conversion efficiency in a given mode can be computed as (see Supplementary Information for derivation using temporal coupled mode theory)

$$\eta_{k\neq 0} = \frac{2\omega_k \gamma_k |a_k|^2}{\sum_{k'} \omega_{k'} \left(-s_{k'} + \sqrt{2\gamma_{k'}} a_{k'}\right)^2}, \tag{3}$$

where k' indexes over all modes in the system, k denotes any mode that is not coherently pumped, and $\mu \ll \gamma$. The denominator of this expression includes both the input pump power and the power drawn from the amplitude modulator. It is useful to compare the power generation efficiency to the Manley-Rowe (MR) limit[44]. The MR limit describes the optimal efficiency in a difference-frequency generation process where every high-energy pump photon produces a lower-energy signal and idler photon. In the case of the idler mode in our system, the MR limit is then given by ω_T/ω_0 (see Supplementary Information for derivation).

When the system does not reach a steady state, interesting behaviors such as stable limit cycles may exist, which we will also explore.

Chiral energy flow in nonlinear multimode cavities

A key prediction of non-Hermitian point gap topology is the non-Hermitian skin effect (NHSE), which occurs when the hopping reciprocity in a lattice is broken, enabling bulk eigenstates of the Hamiltonian to be localized on the boundary of the lattice[45–47]. In one dimension, the Hatano-Nelson model is a simple example exhibiting the NHSE, where reciprocity is broken via unequal nearest-neighbor rightward and leftward hoppings[48,49]. In our system, we realize a nonlinear analog of the Hatano-Nelson model, where nonlinear Hermitian coupling and non-Hermitian amplitude modulation combine to give non-reciprocal hopping amplitudes in the frequency dimension. In Fig. 1b, c, we show how this can result in unidirectional (or chiral) energy flow towards the lowest-frequency mode in our frequency lattice. This chiral energy flow is not accessible with conventional optical nonlinearity or electro-optic modulation on its own.

The chiral energy flow is associated with the formation of an asymmetric frequency comb centered around ω_0. As described in Methods, we can quantify the comb asymmetry as

$$\xi = \frac{\log|r_1| + \log|r_2|}{2\log|r_2|}, \tag{4}$$

where we analytically solve the steady state of Eq. (2) using a non-Hermitian Bloch wave ansatz $a_{-n+1} = r_2 a_{-n}$, $a_{n+1} = r_1 a_n$ for the blue-shifted ($n<0$) and redshifted ($n>0$) branches of the comb, respectively.

We now show how the asymmetry in the frequency comb can be controlled through the interplay between nonlinear and non-Hermitian coupling. In Fig. 2a, we plot the asymmetry parameter ξ over a sweep of the quality factor of the frequency comb modes Q_0. When the comb modes are very leaky (low Q_0), the nonlinear coupling remains weak and a symmetric comb is created through the amplitude modulation (Fig. 2b, (I)). As Q_0 is increased, nonlinear energy can more effectively flow in the frequency space lattice. The asymmetry initially increases slowly, then undergoes a sharp increase as the redshifted part of the comb ($n>0$) is pulled upwards. This occurs because $\beta a_T \to \kappa$, amplifying coupling to lower-frequency modes while simultaneously suppressing the nearest-neighbor hopping to higher-frequency modes.

When the asymmetry reaches $\xi = 0.5$, hopping to higher frequency modes is completely suppressed, $\kappa = \beta a_T$, and a flat comb for the redshifted cascading orders is created through a balance between gain and loss for each mode. The steady state energy of the blueshifted modes continue to decay from the pump mode ω_0 as $|r_2|^{-2|n|}$ (Fig. 2b, (II)). For the highest Q_0 considered, nearly perfect asymmetry in the frequency comb is generated (Fig. 2b, (III)). The interference pattern in the steady state modal energy distribution for this last case is due to Bloch interference in the frequency lattice that emerges because the boundaries of this system in the frequency dimension are not impedance matched (i.e., are partially reflecting)[50]. The interference exists because we only change Q_0 in these simulations, but can be removed

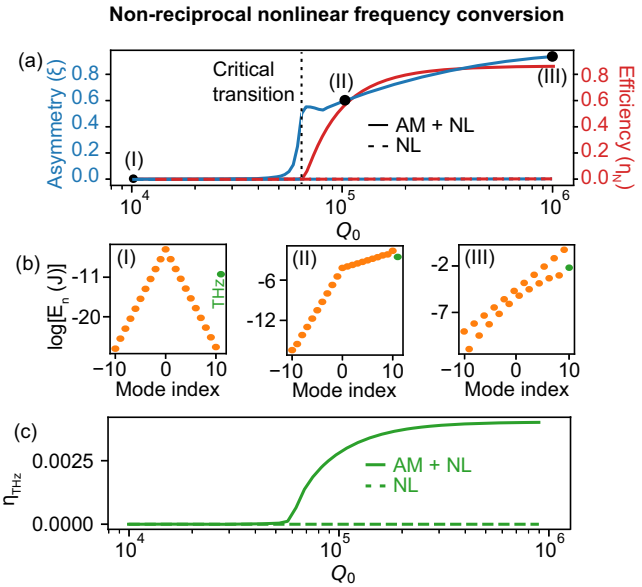

Fig. 2 | Asymmetric and highly efficient frequency conversion through non-reciprocal frequency conversion. a For low Q_0 (strong dissipation in comb modes), the nonlinear coupling is very weak and AM creates a symmetric comb, $\xi \approx 0$ (because $\gamma \gg \kappa$, modes other than the pump mode are negligibly occupied). As Q_0 is increased, the interplay between AM and NL begins to dominate the system dynamics, entering the regime of a high-finesse cavity in frequency space and suppressing frequency upconversion through nonreciprocity. This biases the frequency comb towards redshifted modes. Finally, for the highest Q_0, nearly complete asymmetry is obtained, $\xi \approx 1$. The efficiency parameter η_N quantifies how much power is converted into the chiral mode. A sharp increase near the transition to high asymmetry ($\xi \approx 0.5$) is observed. **b** Varying levels of asymmetry in the modal energy distribution for three different values of the Q_0 sweep shown in (**a**). The interference pattern in (III) emerges due to non-open boundary conditions at the frequency boundaries $\omega_{\pm N}$, which results in Bloch mode interference in the frequency space lattice. **c** As the asymmetry is increased through improving the finesse of the frequency space cavity, so too is the THz conversion efficiency. The non-reciprocity strongly biases THz generation (downconversion) over THz annihilation (upconversion) processes. In these simulations, $\hbar\omega_0|s_0|^2 = 1$ MW, $\beta_0 = 10^{-4}$ J$^{-1/2}$, $\kappa = 2\pi \cdot 1060$ MHz, $Q_T = 10^4$, and $N = 10$. An intrinsic loss $\mu = 0.01\gamma$ was assumed. In the absence of AM (NL only), a seed $\hbar\omega_T|s_T|^2 = 760$ W was added to form the frequency comb, matching the drive power necessary to ensure $J \sim 0.1$ in the presence of AM. Here, $\omega_0 = 2\pi \cdot 282$ THz, $\omega_T = 2\pi \cdot 1.06$ THz. In (**c**), in the limit $\mu \to 0$, η_{THz} for the NL only case ranges from 8×10^{-8} to 6×10^{-6} over the range of Q_0, effectively zero on the plot.

by additionally tuning the boundary condition Q_N for example (as shown in the Supplementary Information).

Also shown in Fig. 2a is a plot of the power conversion efficiency for the chiral mode η_N. We observe a sharp increase in η_N near the transition to high asymmetry. η_N asymptotes near 86% for high Q_0, which is orders of magnitude larger than the efficiency for a system with only nonlinearity and no amplitude modulation. Note that the latter system requires a seed to generate comb modes and the THz idler mode, so we set $\hbar\omega_T|s_T|^2$ equal to the input power of the drive for amplitude modulation in the former system at a modulation index $J \sim 0.1$ (see Supplementary Information for details).

High efficiency terahertz generation

The unidirectional energy flow enabled by non-reciprocal frequency conversion in the frequency dimension biases frequency down-conversions that produce idler photons at ω_T (and suppresses frequency upconversions that annihilate idler photons) in the cascaded nonlinear system. When ω_T lies at THz frequency, the system can realize high efficiency THz generation.

This concept is shown in Fig. 2c, where the efficiency of conversion into the propagating THz idler mode outcoupled from the cavity increases with Q_0. Notice that the curve of THz efficiency plateaus near $\xi \approx 0.5$. At this value of the asymmetry parameter, upconversions are perfectly suppressed, a flat IR comb is generated, and THz generation is enhanced by the number of comb modes. Here, the THz photon generation rate is equally contributed by three-wave mixing between each pair of nearest-neighbor comb modes. As Q_0, ξ increases, the THz generation becomes dominated by three-wave mixing at the low frequency end of the frequency comb, which is populated strongly due to the non-reciprocal frequency conversion.

We observe an order of magnitude enhancement in THz conversion efficiency for the non-reciprocal frequency comb compared to the reciprocal frequency comb without amplitude modulation. We attribute this enhancement to the unique ability to suppress upconversions in the non-Hermitian system and therefore break symmetry between THz-generating and THz-annihilating processes. The critical transition to high asymmetry and chiral mode efficiency (black dotted line in Fig. 2a) is accompanied by a transition to high THz conversion efficiencies.

In Fig. 3, we explore how THz conversion efficiencies strongly surpassing the Manley-Rowe limit can be achieved through (1) longer combs and (2) appropriate dissipation engineering, reaching enhancement factors exceeding 32 times above the Manley-Rowe limit ($\eta_{THz} > 12\%$). The former enables more cascading steps to generate THz photons from a single pump photon, while the latter shapes the steady state energy distribution in the frequency lattice to maximize THz-generating nonlinear interactions. In Fig. 3, the dissipation engineering corresponds to partially open boundary conditions and low occupation of the blueshifted comb modes (which correspond to THz annihilation processes). As noted in the Supplementary Information, dissipation engineering is another resource to control nonlinear energy flow, and new capabilities can arise when dissipation engineering is combined with non-reciprocal frequency conversion.

Note that in Fig. 3 we simulate a pump power of 10 kW, which is achievable with microsecond pulses. This is too low to generate appreciable THz using cascaded nonlinear conversion alone, but nevertheless achieves high η_{THz} when combined with amplitude modulation to break reciprocity in nonlinear frequency conversion. This highlights the ability of our mechanism to overcome the conventional limitations of high pump power that usually plagues high-efficiency frequency generation owing to the weakness of optical nonlinearity. The high-power THz generation in the nonlinear, non-Hermitian system is enabled through the interplay between optical nonlinearity and non-Hermitian coupling between frequency modes. Although chiral energy flow can be achieved through combined amplitude and phase modulation without optical nonlinearity (as described in the Supplementary Information), the latter is necessary to simultaneously generate idler photons with high efficiency. It is this nonlinear coupling that actually makes the comb robust to chiral energy flow towards lower frequency instead of higher frequency. Reciprocity is only broken when $|\beta a_T| \sim |\kappa|$, which necessitates preference towards downconversion processes that generate idler photons. Thus, chiral energy flow towards higher energy is not generally allowed by this mechanism, but can be accessed using combined amplitude and phase modulation (see Supplementary Information).

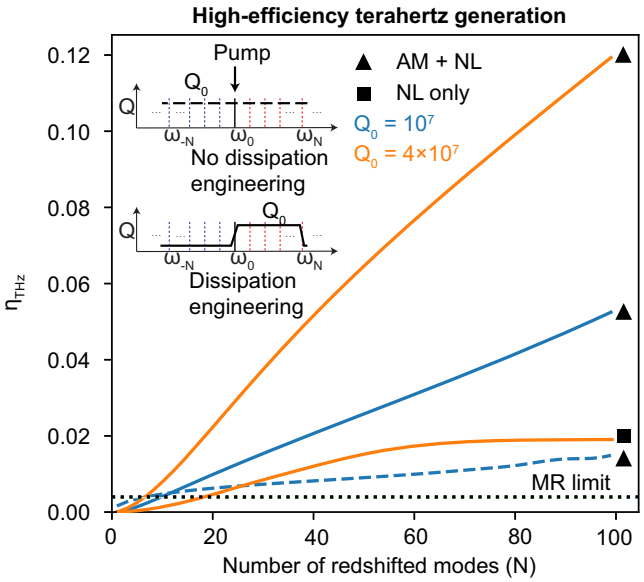

Fig. 3 | Breaking the Manley-Rowe limit through non-reciprocal frequency conversion. Efficiency of terahertz idler mode generation η_{THz} as a function of comb length with (solid lines) and without (dashed line) dissipation engineering, showing strong enhancement with respect to the Manley-Rowe (MR) limit. In these simulations, $\hbar\omega_0|s_0|^2 = 10$ kW, $\beta_0 = 3 \times 10^{-4}$ J$^{-1/2}$, $\Delta = 2\pi \cdot 6.34$ MHz, $Q_T = 10^4$, and $\mu = 10^{-2}\gamma$. With dissipation engineering, the pump and boundary modes have quality factor $Q_N = 4 \times 10^5$ and the blueshifted modes have quality factor $Q_b = 10^2$. The case with only nonlinearity (NL only) included a seed $\hbar\omega_T|s_T|^2 = 0.484$ mW, equal to the THz drive power necessary for modulation index $J \sim 0.03$ (free spectral range FSR = 1 GHz) in the presence of amplitude modulation. The following efficiencies are not shown because they are effectively zero on the plot: $\eta_{THz} \approx 0$ (NL only with $Q_0 = 10^7$, 4×10^7 and no dissipation engineering), $\eta_{THz} = 1.38 \times 10^{-7}$ (NL only with $Q_0 = 10^7$ and dissipation engineering). The case for the non-reciprocal system (AM + NL) with $Q_{max} = 4 \times 10^7$ without dissipation engineering is not plotted because it did not reach a steady state within 1 μs.

Robustness to defect and disorder

In this section, we show how the non-reciprocal frequency conversion we observe in the frequency dimension preserves the robustness to disorder observed for NHSE[51]. In Fig. 4a, we introduce a random leaky mode in the frequency mode, which has a Q factor lower than the other modes in the comb, $Q_{defect} < Q_0$. The original skin effect is preserved for large defect strengths, even when the defect mode has a Q factor over 90% below Q_0. When the defect mode becomes too leaky ($Q_{defect}/Q_0 \lesssim 1\%$), the comb terminates at the defect mode, and the new chiral mode becomes the comb mode just before the defect mode.

In Fig. 4b, we consider disorder in the Q factor distribution for all of the frequency modes in the comb. To model this disorder, we sample each mode's Q factor individually and uniformly from the distribution $[xQ_0, Q_0]$ with $0 \le x \le 100\%$. We see how the skin effect is resistant to disorder, preserving the unidirectional flow of energy in frequency space even for large amounts of disorder $1 - x > 50\%$. To show that this emerges from the non-Hermitian coupling in the

https://doi.org/10.1038/s41467-025-62853-0

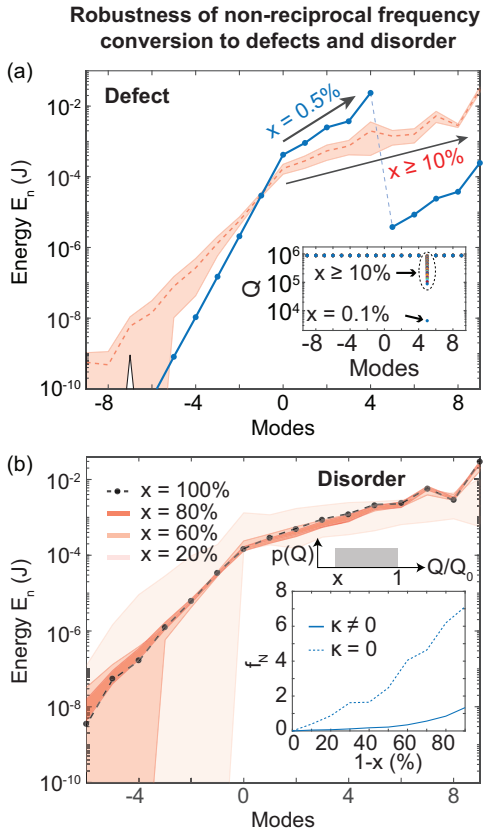

Fig. 4 | Robustness of non-reciprocal frequency conversion to defect and disorder. a A random low Q-factor defect is introduced in the frequency comb. The non-reciprocal frequency conversion is robust to strong defects, though the strongest defects result in the skin effect terminating just before the defect mode. Here, the modal energy $E_n = \hbar\omega_n|a_n|^2$ is plotted for various defect strengths $Q_{\text{defect}}/Q_0 = x$, where Q_0 denotes the Q factor of the remaining modes in the frequency comb. **b** Robustness of non-reciprocal frequency conversion to disorder. Here, the Q factor of all frequency modes in the comb is sampled uniformly from $[xQ_0, Q_0]$. $N_{\text{samp}} = 100$ samples are drawn from this uniform distribution and individually simulated, with the shaded regions denoting $\pm 1\sigma$ standard deviation from the mean modal energies. Shown in the inset is the robustness of the energy of the chiral mode a_N, plotted as the standard deviation normalized by the mean (coefficient of variation), $f_N \equiv \sigma_N/\langle E_N\rangle$, where $\langle E_N\rangle$ denotes the ensemble average over N_{samp} samples. In the absence of amplitude modulation $\kappa = 0$, the disorder affects f_N much more strongly than the case $\kappa \neq 0$, where reciprocity breaking helps stabilize the modal energy in the chiral mode. System parameters include $2N+1 = 19$, $\beta_0 = 5\times10^{-4}\ \text{J}^{-1/2}$, $\kappa = 2\pi\cdot 350$ MHz, $Q_0 = 8.86\times10^9$, $Q_T = 500$, $\mu = 0.9\gamma$, $\hbar\omega_0|s_0|^2 = 5$ MW, $\omega_0 = 2\pi\cdot 282$ THz, and $\omega_T = 2\pi\cdot 1.06$ THz.

system, we plot in the inset of Fig. 4b the standard deviation in the modal energy of the chiral mode normalized to its mean in the presence ($\kappa \neq 0$) and absence ($\kappa = 0$) of amplitude modulation. (The mean and standard deviation are computed over 100 simulated systems with Q factors drawn from the aforementioned uniform Q factor distribution.) The variation in the chiral mode's energy is larger and scales more sharply with the dimensionless disorder parameter x in the case $\kappa = 0$, showing the robustness of the non-reciprocal frequency conversion ($\kappa \neq 0$) to the disorder considered here. This can have a very strong impact for practical applications conventionally limited by dispersion or impurities. In the Supplementary Information, we explore how the system's non-reciprocal frequency conversion remains robust to comb-cavity mode detuning and dispersion. However, the shaping of the comb profile by dispersion suggests dispersion engineering as an exciting tool, together with the dissipation and non-reciprocity engineering we have explored here, to enable precise control over energy flow in frequency dimensions.

Temporal dynamics and stable limit cycles

We now take a closer look at the temporal dynamics of states supported by the nonlinear, non-Hermitian multimode systems considered here. In Fig. 5, we show how these states can generally be classified as steady state solutions or limit cycles (LCs). Thus far, we have focused on combs generated in steady state. LCs are a particularly interesting class of solutions unique to nonlinear systems that are characterized by stable oscillations around a fixed point[52]. As shown in Fig. 5a, the LC regime can be entered by gradually increasing the quality factor of the idler mode, Q_T. The steady state solutions are distinguished by an approach to equilibrium characterized by damped relaxation oscillations (ROs) and Bloch oscillations, whereas the limit cycle regime is characterized by periodic oscillations in the modal amplitudes that never relax to a steady state. We numerically verified the existence of a fixed point in between the extrema of the LCs. Zooming in on the LC regime, we observe that the repetition rate of the LCs appears to be governed by the amplitude modulation strength κ, while the pulse width is governed by the interplay between on-site loss and gain/loss due to intermodal coupling. For each individual mode, the LCs resemble picosecond pulses with GHz repetition rates. The high powers in this system, particularly near the LC regime, are limited by nonlinear saturation effects, which we model in our simulations by inclusion of a two-photon absorption term in the rate equations with $\beta_{\text{TPA}} \sim 0.1$ cm/GW.

We can sweep over the nonlinear and amplitude modulation strengths β, κ to create a phase diagram portraying the distinct temporal dynamics, as shown in Fig. 5b. For small κ, symmetric combs are produced in a steady state irrespective of β (reciprocal frequency conversion, RFC SS). As κ is increased, the non-reciprocal frequency conversion drives the system towards an asymmetric comb in steady state (NRFC SS). The nonlinearity acts as a loss mechanism to balance the gain from amplitude modulation, so that for small nonlinearity β, gain induced by κ drives the system to very high powers that would be limited by nonlinear saturation effects (e.g., TPA). Finally, the largest values of κ in nonlinearity-stabilized systems yield LCs. Like the sharp transition to non-reciprocal frequency conversion, the transition to LCs appears to be quite sensitive to κ, switching sharply from steady state solutions to LCs for almost all values of β. Therefore, beyond a certain threshold, the amplitude modulation stabilizes the LCs, and the LC phenomenon is relatively insensitive to the nonlinear strength. The phase transition boundary is characterized by sustained Bloch oscillations in the frequency space cavity defined by the frequency comb, as shown in the inset[53]. These oscillations resemble solitons in a frequency dimension, where nonlinear energy flow bounces back and forth inside the frequency space cavity (outside of the LC regime, these oscillations are damped and relax to a steady state).

Finally, in Fig. 5c, we explore the power in the outcoupled field $s_{\text{out}}(t) = \sum_n s_{n,\text{out}}(t)e^{-i\omega_n t}$. Both the RFC and NRFC SS phases can show approximate continuous wave operation when one mode has most of the system's energy (the pump mode (blue) in the former case, the frequency-shifted chiral mode (red) in the latter case). NRFC SS can additionally create flat combs with sinc-type pulse profiles (orange). The LC regime features pulses with GHz repetition rate and THz subpulse dynamics, providing the opportunity to encode information at two different timescales in the optical field.

Discussion

The interplay between nonlinearity and non-Hermitian coupling in the frequency comb systems studied here offers numerous exciting avenues of research for both fundamental science and photonic applications. First, the non-reciprocal frequency conversion we explore enables long-range frequency shifting, realizing coherent sources whose frequency can be tuned simply by shifting the boundary condition along the frequency dimension. In the quantum optical regime, the interaction between optical nonlinearity and non-Hermiticity

https://doi.org/10.1038/s41467-025-62853-0

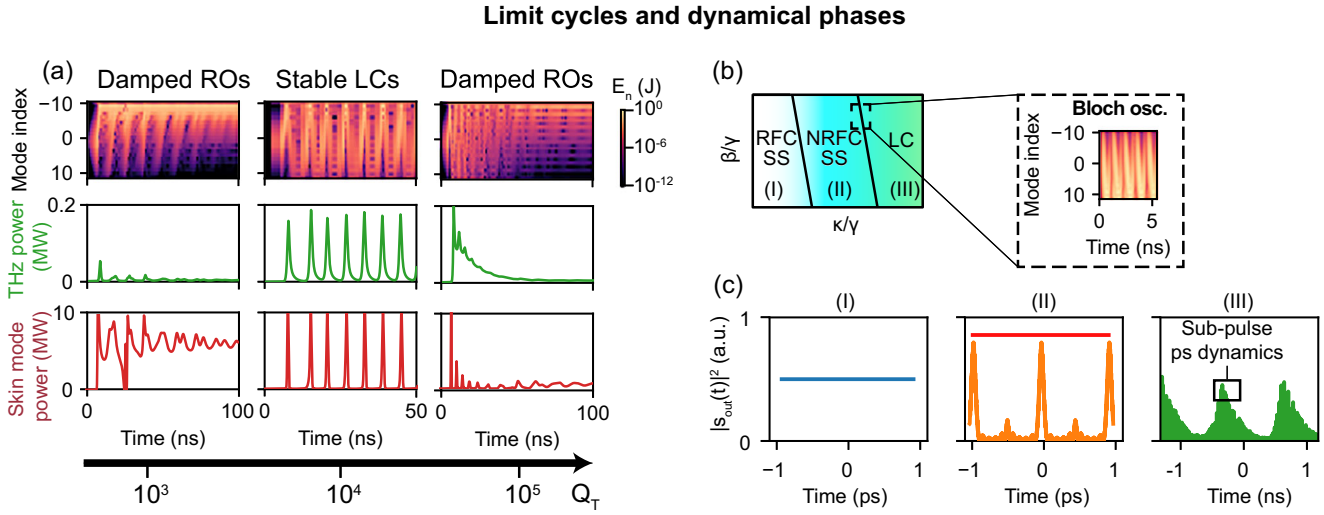

Fig. 5 | Limit cycles and temporal dynamics in nonlinear, non-Hermitian multimode systems. a For low quality factors of the idler bath mode (Q_T), the system initially features damped relaxation oscillations (ROs) and the amplitude modulation drives the system towards a stable steady state that features non-reciprocal frequency conversion. As Q_T increases, the system eventually transitions into a regime of stable limit cycles that feature periodic oscillations in modal energy. Finally, larger Q_T cause a return back to damped ROs and Bloch oscillations, with the nonlinearity and amplitude modulation enabling a gain-loss equilibrium. Oscillations in modal energy in the limit cycle regime have a GHz repetition rate, roughly corresponding to the amplitude modulation strength κ. **b** Phase diagram showing steady state (SS) and limit cycle (LC) regimes as a function of the nonlinear and amplitude modulation strengths. For small κ, a symmetric comb in steady state is produced (ξ, $\eta \approx 0$, with reciprocal frequency conversion (RFC SS)). For larger κ, an asymmetric comb in steady state is produced by the non-reciprocal frequency conversion (NRFC SS, ξ, $\eta > 0$). For the largest κ, LCs are present. Along the transition boundary, the temporal dynamics feature long-lasting Bloch solitons where energy bounces back and forth in the frequency space cavity. **c** Representative time traces of the power in the outcoupled field $s_{out}(t) = \sum_n s_{n,out}(t) e^{-i\omega_n t}$ corresponding to the phases in (**b**). Simulation parameters used in (a) are $Q_0 = 1.1 \times 10^7$, $\kappa = 2\pi \cdot 100$ MHz, $\beta_0 = 10^{-4}$ J$^{-1/2}$. The pump power is 1 kW and the comb length is $2N + 1 = 21$.

remains to be explored and may enable the creation of topologically-protected multimode quantum and non-Gaussian states of light[54]. In addition, tailoring non-reciprocal hopping in a frequency dimension offers an exciting resource for quantum walk studies. Furthermore, the multimode limit cycles explored in this work, in addition to being used for multi-frequency pump-probe spectroscopy and time multiplexing, suggest the possibility of harnessing multistability for switching, entangled state generation, and more[55]. Finally, we envision that combining non-reciprocal conversion with techniques such as dissipation engineering[10,56] will lead to even more precise control over nonlinear energy flow in multimode systems.

We briefly comment on experimental platforms capable of realizing the effects described here. Most of the systems we simulate in the main text are based on centimeter-scale free space/monolithic cavities pumped by microsecond pulsed or nanosecond Q-switched lasers, which realize quasi-continuous wave operation at kilowatt and megawatt-level powers, respectively. A further discussion of typical parameters expected in this platform is provided in the Supplementary Information. The THz amplitude modulation (AM) we consider can come in two forms (1) externally-driven AM and (2) self-driven AM. In the first case, a weak THz drive (to ensure a modulation index $J \ll 1$) is injected into the AM. The steady state THz energies are several orders of magnitude larger, showcasing the ability of our system to generate high-energy THz radiation from a weak THz seed with high efficiency. In the second case, no external THz radiation is injected into the cavity. Rather, the system is pumped and seeded at two infrared frequencies to initiate the cascaded three-wave mixing, and the resulting THz photons are recycled to drive the AM. We provide a more detailed discussion with specific results for this case in the Supplementary Information. To our knowledge, this is the first proposal of intracavity terahertz amplification by recycling idler photons for electro-optic modulation in an optically driven cavity. Exciting steps in this direction have been taken in demonstrations of THz time-domain electro-optic sampling[57].

Ring resonators have recently received significant attention in studies of topological effects in synthetic frequency dimensions[29,58,59]. For example, one such system used Mach-Zehnder-based amplitude modulation of a fiber ring resonator to realize non-Hermitian band topology. We view this platform as an excellent candidate to realize the effects described here when combined with lithium niobate photonics (or another nonlinear material) to generate nonlinear coupling. On-chip nonlinear microring resonators have also been extensively developed and suggest exciting potential for developing integrated non-reciprocal frequency conversion setups[60–62]. Advances in THz electro-optic modulation further suggest exciting possibilities for using THz amplitude modulators to generate the THz-spaced non-reciprocal combs considered in this work[63–65].

We emphasize that our theory is applicable to different frequency regimes. In particular, THz modulation frequencies were considered here to highlight the well-known difficulty in high-efficiency THz generation that our mechanism addresses. However, optomechanical and circuit quantum electrodynamics platforms are ideal platforms to realize the physics described here at microwave frequencies[66]. Furthermore, MHz/GHz amplitude modulation with THz-based cascaded nonlinearity can lead to excitation of long-range Bloch modes, band structures with very large winding numbers, and formation of a series of flat combs at IR and mid-IR/THz frequencies, as described in the Supplementary Information. Exploiting these two disparate frequency ranges offers the potential for exploring higher-dimensional non-Hermitian topology.

In summary, we have uncovered the phenomenon of non-reciprocal frequency conversion in multimode systems supporting simultaneous non-Hermitian and nonlinear intermodal coupling. We envision widespread adoption of the physical concepts described here in both fundamental studies of non-Hermitian topology in nonlinear systems as well as applications to new classes of high-efficiency nonlinear photonic devices.

Methods

Hamiltonian description of multimode nonlinear system

The non-interacting multimode driven-dissipative Hamiltonian describing our system is the sum of the bare Hamiltonians for each mode and reads[67]:

$$\begin{aligned}\mathcal{H}_0/\hbar = i\sqrt{2\gamma}s_0(\hat{a}_0^\dagger - \hat{a}_0) + \sum_n [\omega_n - i(\gamma+\mu)]\hat{a}_n^\dagger \hat{a}_n \\ + [\omega_T - i(\gamma_T+\mu_T)]\hat{a}_T^\dagger \hat{a}_T,\end{aligned} \tag{5}$$

where $\hat{a}_n$ is the annihilation operator for the comb mode at angular frequency ω_n and $\hat{a}_T$ is the annihilation operator for the idler bath mode at frequency ω_T. This Hamiltonian is non-Hermitian due to on-site loss (γ for outcoupling loss and μ for intrinsic loss) that emerges from the coupling of each frequency mode to the environment. Here, we only consider the mode at ω_0 to be externally pumped ($s_0 \neq 0$). The nonlinear interaction between the frequency modes is described by a Hermitian Hamiltonian[68]

$$\mathcal{H}_{\mathrm{NL}} = i\beta \sum_n \hat{a}_T^\dagger \hat{a}_n^\dagger \hat{a}_{n-1} + \mathrm{h.c.}, \tag{6}$$

where h.c. denotes the Hermitian conjugate, and, as noted in the main text, we drop the frequency dependence of β for simplicity in the mathematical expressions. We now add amplitude modulation at the frequency $\omega_{\mathrm{mod}} = \omega_T$ to this system, generating an anti-Hermitian Hamiltonian[69]

$$\mathcal{H}_{\mathrm{A}} = i\kappa \sum_n \hat{a}_n^\dagger \hat{a}_{n-1} - \mathrm{h.c.}. \tag{7}$$

We consider the case $\omega_{\mathrm{mod}} \ll \omega_T$ in the Supplementary Information (SI), demonstrating a completely distinct regime of operation. Here, the composite Hamiltonian $\mathcal{H} = \mathcal{H}_0 + \mathcal{H}_{\mathrm{NL}} + \mathcal{H}_{\mathrm{A}}$ is non-Hermitian and, from it, we can derive Heisenberg equations of motion in the mean field for the annihilation operators $\hat{a}_n, \hat{a}_T$, as quoted in the main text:

$$\begin{aligned}\dot{a}_T &= \beta \sum_k a_k^* a_{k-1} - (\gamma_T + \mu_T)a_T \\ \dot{a}_n &= -(\beta^* a_T + C^* - \kappa^*)a_{n+1} + (\beta a_T^* + C + \kappa)a_{n-1} - (\gamma_n + \mu_n)a_n + \sqrt{2\gamma_n}s_n.\end{aligned} \tag{8}$$

where $s_{n\neq 0} = 0$. Here, we include for completeness the Hermitian coupling C that can be achieved through phase modulation, though, for examples in the main text, $C = 0$. An example of asymmetric comb generation using amplitude and phase modulation is provided in the Supplementary Information.

Two-level model with onsite gain and loss

In this section, we show how the non-Hermitian coupling in the multimode nonlinear system manifests as gain and loss. Considering a two-mode basis for neighboring modes $\{a_n, a_{n+1}\}$, we can write the unit cell Hamiltonian as

$$\begin{aligned}\mathcal{H} &= \begin{pmatrix} \omega_0 - i\gamma & \kappa + \beta a_T \\ \kappa - \beta a_T & \omega_0 - i\gamma \end{pmatrix} \\ &= (\omega_0 - i\gamma)\mathbf{I} + \begin{pmatrix} 0 & \kappa + \beta a_T \\ \kappa - \beta a_T & 0 \end{pmatrix}.\end{aligned} \tag{9}$$

One can think of this Hamiltonian as the one-photon transition matrix in the synthetic frequency dimension. Denote the basis in which this Hamiltonian is written $\{|0\rangle, |1\rangle\}$ such that $|0\rangle \equiv a_n^\dagger|\mathrm{vac}\rangle$, $|1\rangle \equiv a_{n+1}^\dagger|\mathrm{vac}\rangle$, where $|\mathrm{vac}\rangle$ denotes the (multimode) vacuum state. The matrix elements of H can be derived as $\langle m|\mathcal{H}|n\rangle$, with $\mathcal{H}$ the composite Hamiltonian written above.

Performing a change of basis $|0\rangle, |1\rangle \to \frac{|0\rangle \pm i|1\rangle}{\sqrt{2}}$, we find the interaction Hamiltonian now reads

$$\mathcal{H}'_{\mathrm{int}} = \begin{pmatrix} -i\beta a_T & i\kappa \\ -i\kappa & i\beta a_T \end{pmatrix}, \tag{10}$$

so that the nonlinearity now manifests as on-site gain and loss, and the amplitude modulation acts as a Hermitian coupling.

Asymmetry parameter for non-reciprocal frequency conversion

To quantify the asymmetry in the redshifted and blueshifted branches of the comb around the pump mode ω_0, we will assume a long frequency comb with negligible boundary effects (see Supplementary Information for boundary-related effects and further details on the following method). In this case, we can solve the rate equations in steady state using an ansatz $a_{n+1} \propto r_1 a_n$, $a_{-n+1} \propto r_2 a_{-n}$, respectively, for the redshifted and blueshifted branches ($n > 0$ here). This ansatz is physically motivated by the non-Hermitian analog of Bloch bands (where in the Hermitian case $r_1 = r_2 = e^{ik}$ with k the wavenumber). Both r_1, r_2 must satisfy the steady state condition

$$(\kappa - \beta a_T)r + (\kappa + \beta a_T)r^{-1} - \gamma = 0, \tag{11}$$

where a_T denotes the steady state THz mode amplitude. From the solutions of this equation (see Supplementary Information), we can calculate the asymmetry parameter ξ used in the main text. Graphically, in a logarithmic plot of modal energy, ξ represents a normalized ratio of the sum of the slopes of the redshifted ($2|r_1|$) and blueshifted ($2|r_2|$) branches. When amplitude modulation is absent and dissipation exceeds the nonlinear rate ($\kappa = 0$, $\gamma \gg |\beta a_T|$), a symmetric comb with $\xi = 0$ is generated. When the strength of amplitude modulation approaches the nonlinear rate, $\kappa \sim \beta a_T$, reciprocity is broken in the upconversion and downconversion processes, biasing energy flow towards redshifted modes and creating an asymmetric comb with $\xi \neq 0$. We confirmed the validity of ξ as a figure of merit for asymmetry by numerically performing exponential fits to the modal energy distributions (see Supplementary Information for details).

Data availability

All data supporting this work are available within the manuscript or the Supplementary Information.

Code availability

Simulation code is made publicly available at https://github.com/sahil271828/nrfc/tree/main.

References

1. Fejer, M. M. Nonlinear optical frequency conversion. *Phys. Today* **47**, 25 (1994).
2. Boyd, R. W., Gaeta, A. L. & Giese, E. in *Springer Handbook of Atomic, Molecular, and Optical Physics* (Springer, 2008).
3. Schneider, T. *Nonlinear Optics in Telecommunications*. (Springer Science & Business Media, 2013).
4. Chang, D. E., Vuletić, V. & Lukin, M. D. Quantum nonlinear optics-photon by photon. *Nat. Photonics* **8**, 685 (2014).
5. Caspani, L. et al. Integrated sources of photon quantum states based on nonlinear optics. *Light Sci Appl* **6**, e17100 (2017).
6. Picqué, N. & Hänsch, T. W. Frequency comb spectroscopy. *Nat. Photonics* **13**, 146 (2019).
7. Marin-Palomo, P. et al. Microresonator-based solitons for massively parallel coherent optical communications. *Nature* **546**, 274 (2017).
8. Corcoran, B. et al. Ultra-dense optical data transmission over standard fibre with a single chip source. *Nat. Commun.* **11**, 2568 (2020).
9. Ravi, K. et al. Cascaded parametric amplification for highly efficient terahertz generation. *Opt. Lett.* **41**, 3806 (2016).

10. Salamin, Y. et al. Overcoming the manley-rowe limit for cw terahertz generation in q-engineered multimodal cavity. In *CLEO: QELS_Fundamental Science* (Optica Publishing Group, 2021).
11. Olgun, H. T. et al. Highly efficient generation of narrowband terahertz radiation driven by a two-spectral-line laser in ppln. *Opt. Lett.* **47**, 2374 (2022).
12. Suh, J. et al. Photonic topological spin pump in synthetic frequency dimensions. *Phys. Rev. Lett.* **132**, 033803 (2024).
13. Flower, C. J. et al. Observation of topological frequency combs. *Science* **384**, 1356 (2024).
14. Mittal, S., Moille, G., Srinivasan, K., Chembo, Y. K. & Hafezi, M. Topological frequency combs and nested temporal solitons. *Nat. Phys.* **17**, 1169 (2021).
15. Sounas, D. L. & Alù, A. Non-reciprocal photonics based on time modulation. *Nat. Photonics* **11**, 774 (2017).
16. Caloz, C. et al. Electromagnetic nonreciprocity. *Phys. Rev. Appl.* **10**, 047001 (2018).
17. Yuan, L., Lin, Q., Xiao, M. & Fan, S. Synthetic dimension in photonics. *Optica* **5**, 1396 (2018).
18. El-Ganainy, R., Khajavikhan, M., Christodoulides, D. N. & Ozdemir, S. K. The dawn of non-hermitian optics. *Commun. Phys.* **2**, 37 (2019).
19. Asadchy, V. S., Mirmoosa, M. S., Díaz-Rubio, A., Fan, S. & Tretyakov, S. A. Tutorial on electromagnetic nonreciprocity and its origins. *Proc. IEEE* **108**, 1684 (2020).
20. Lustig, E. & Segev, M. Topological photonics in synthetic dimensions. *Adv. Opt. Photonics* **13**, 426 (2021).
21. Wang, C. et al. Non-hermitian optics and photonics: from classical to quantum. *Adv. Opt. Photonics* **15**, 442 (2023).
22. Li, A. et al. Exceptional points and non-hermitian photonics at the nanoscale. *Nat. Nanotechnol.* **18**, 706 (2023).
23. Parto, M., Liu, Y. G., Bahari, B., Khajavikhan, M. & Christodoulides, D. N. Non-hermitian and topological photonics: optics at an exceptional point. *Nanophotonics* **10**, 403 (2020).
24. Miri, M.-A. & Alu, A. Exceptional points in optics and photonics. *Science* **363**, eaar7709 (2019).
25. Feng, L., El-Ganainy, R. & Ge, L. Non-hermitian photonics based on parity–time symmetry. *Nat. Photonics* **11**, 752 (2017).
26. Song, Y. et al. Two-dimensional non-hermitian skin effect in a synthetic photonic lattice. *Phys. Rev. Appl.* **14**, 064076 (2020).
27. Zhu, X. et al. Photonic non-hermitian skin effect and non-bloch bulk-boundary correspondence. *Phys. Rev. Res.* **2**, 013280 (2020).
28. de Castro, P. F. & Benalcazar, W. A. Solitons with self-induced topological nonreciprocity. Preprint at https://doi.org/10.48550/arXiv.2405.14919 (2024).
29. Wang, K. et al. Generating arbitrary topological windings of a non-hermitian band. *Science* **371**, 1240 (2021).
30. Wang, K., Dutt, A., Wojcik, C. C. & Fan, S. Topological complex-energy braiding of non-hermitian bands. *Nature* **598**, 59 (2021).
31. Shen, Z. et al. Nonreciprocal frequency conversion and mode routing in a microresonator. *Phys. Rev. Lett.* **130**, 013601 (2023).
32. Many Manda, B., Carretero-González, R., Kevrekidis, P. G. & Achilleos, V. Skin modes in a nonlinear hatano-nelson model. *Phys. Review B* **109**, 094308 (2024).
33. Sloan, J., Vaidya, S., Rivera, N. & Soljačić, M. Noise immunity in quantum optical systems through non-hermitian topology. Preprint at https://doi.org/10.48550/arXiv.2405.14919 (2025)
34. Fang, K. et al. Generalized non-reciprocity in an optomechanical circuit via synthetic magnetism and reservoir engineering. *Nat. Phys.* **13**, 465 (2017).
35. Peterson, G. A. et al. Demonstration of efficient nonreciprocity in a microwave optomechanical circuit. *Phys. Rev. X* **7**, 031001 (2017).
36. Xu, X.-W., Song, L., Zheng, Q., Wang, Z. & Li, Y. Optomechanically induced nonreciprocity in a three-mode optomechanical system. *Phys. Rev. A* **98**, 063845 (2018).
37. Shen, Z. et al. Experimental realization of optomechanically induced non-reciprocity. *Nat. Photonics* **10**, 657 (2016).
38. Xu, H., Jiang, L., Clerk, A. & Harris, J. Nonreciprocal control and cooling of phonon modes in an optomechanical system. *Nature* **568**, 65 (2019).
39. Miri, M.-A., Ruesink, F., Verhagen, E. & Alù, A. Optical nonreciprocity based on optomechanical coupling. *Phys. Rev. Appl.* **7**, 064014 (2017).
40. Xu, X.-W. & Li, Y. Optical nonreciprocity and optomechanical circulator in three-mode optomechanical systems. *Phys. Rev. A* **91**, 053854 (2015).
41. Guo, X., Zou, C.-L., Jung, H. & Tang, H. X. On-chip strong coupling and efficient frequency conversion between telecom and visible optical modes. *Phys. Rev. Lett.* **117**, 123902 (2016).
42. Lugiato, L., Prati, F., Gorodetsky, M. & Kippenberg, T. From the lugiato–lefever equation to microresonator-based soliton kerr frequency combs. *Philos. Trans. R. Soc. A Math. Phys. Eng. Sci.* **376**, 20180113 (2018).
43. Hu, Y. et al. Integrated electro-optics on thin-film lithium niobate. *Nat. Rev. Phys.* **7**, 237–254 (2025).
44. Manley, J. & Rowe, H. Some general properties of nonlinear elements-part i. general energy relations. *Proc. IRE* **44**, 904 (1956).
45. Okuma, N., Kawabata, K., Shiozaki, K. & Sato, M. Topological origin of non-hermitian skin effects. *Phys. Rev. Lett.* **124**, 086801 (2020).
46. Zhang, X., Zhang, T., Lu, M.-H. & Chen, Y.-F. A review on non-hermitian skin effect. *Adv. Phys. X* **7**, 2109431 (2022).
47. Lin, R., Tai, T., Li, L. & Lee, C. H. Topological non-hermitian skin effect. *Front. Phys.* **18**, 53605 (2023).
48. Hatano, N. & Nelson, D. R. Localization transitions in non-hermitian quantum mechanics. *Phys. Rev. Lett.* **77**, 570 (1996).
49. Kawabata, K., Sato, M. & Shiozaki, K. Higher-order non-hermitian skin effect. *Phys. Rev. B* **102**, 205118 (2020).
50. Hu, Y. et al. Mirror-induced reflection in the frequency domain. *Nat. Commun.***13**, 6293 (2022).
51. Claes, J. & Hughes, T. L. Skin effect and winding number in disordered non-hermitian systems. *Phys. Rev. B* **103**, L140201 (2021).
52. Strogatz, S. H. *Nonlinear Dynamics and Chaos: With Applications to Physics, Biology, Chemistry, and Engineering* (CRC Press, 2018)
53. Englebert, N. et al. Bloch oscillations of coherently driven dissipative solitons in a synthetic dimension. *Nat. Phys.* **19**, 1014 (2023).
54. Blanco-Redondo, A., Bell, B., Oren, D., Eggleton, B. J. & Segev, M. Topological protection of biphoton states. *Science* **362**, 568 (2018).
55. Pelka, K., Madiot, G., Braive, R. & Xuereb, A. Floquet control of optomechanical bistability in multimode systems. *Phys. Rev. Lett.* **129**, 123603 (2022).
56. Pontula, S., Salamin, Y., Roques-Carmes, C. & Soljačić, M. Shaping quantum noise through cascaded nonlinear processes in a dissipation-engineered multimode cavity. *PRX Quantum* **5**, 040345 (2024).
57. Salamin, Y. et al. Compact and ultra-efficient broadband plasmonic terahertz field detector. *Nat. Commun.* **10**, 5550 (2019).
58. Dutt, A. et al. A single photonic cavity with two independent physical synthetic dimensions. *Science* **367**, 59 (2020).
59. Lustig, E., Guidry, M. A., Lukin, D. M., Fan, S. and Vuckovic, J., Emerging quadrature lattices of kerr combs. Preprint at http://arxiv.org/abs/2407.13049v1 (2024)
60. Chen, L., Wood, M. G. & Reano, R. M. 12.5 pm/v hybrid silicon and lithium niobate optical microring resonator with integrated electrodes. *Opt. Exp.* **21**, 27003 (2013).
61. Guarino, A., Poberaj, G., Rezzonico, D., Degl'Innocenti, R. & Günter, P. Electro–optically tunable microring resonators in lithium niobate. *Nat. Photon.* **1**, 407 (2007).
62. Zhang, M. et al. Broadband electro-optic frequency comb generation in a lithium niobate microring resonator. *Nature* **568**, 373 (2019).

63. Ma, Z., Geng, Z., Fan, Z., Liu, J. & Chen, H. Modulators for terahertz communication: The current state of the art. *Research* https://doi.org/10.34133/2019/6482975 (2019).
64. Wang, Z. et al. Recent progress in terahertz modulation using photonic structures based on two-dimensional materials. *InfoMat* **3**, 1110 (2021).
65. Couture, N. et al. Terahertz electro-optic modulation of single photons. Preprint at https://doi.org/10.48550/arXiv.2503.19667 (2025).
66. Moon, K. & Girvin, S. Theory of microwave parametric down-conversion and squeezing using circuit qed. *Phys. Rev. Lett.* **95**, 140504 (2005).
67. Gardiner, C. W. & Collett, M. J. Input and output in damped quantum systems: Quantum stochastic differential equations and the master equation. *Phys. Rev. A* **31**, 3761 (1985).
68. Graham, R. & Haken, H. The quantum-fluctuations of the optical parametric oscillator.*Zeitschrift für Phys. A Hadrons Nuclei* **210**, 276 (1968).
69. Yuan, L., Dutt, A. & Fan, S. Synthetic frequency dimensions in dynamically modulated ring resonators. APL Photonics **6**, 071102 (2021).

Acknowledgements

S.P. acknowledges the financial support of the Hertz Fellowship Program and NSF Graduate Research Fellowship Program. Y.S. acknowledges support from the Swiss National Science Foundation (SNSF) through the Early Postdoc Mobility Fellowship No. P2EZP2188091. S.V. and M.S. acknowledge support from the U.S. Office of Naval Research (ONR) Multidisciplinary University Research Initiative (MURI) under Grant No. N00014-20-1-2325 on Robust Photonic Materials with Higher-Order Topological Protection. C.R.-C. is supported by a Stanford Science Fellowship. This material is based upon work supported in part by the Air Force Office of Scientific Research under the award number FA9550-20-1-0115; the work is also supported in part by the U. S. Army Research Office through the Institute for Soldier Nanotechnologies at MIT, under Collaborative Agreement Number W911NF-23-2-0121. This work is additionally supported in part by the DARPA Agreement No. HO0011249049. We also acknowledge the support of Parviz Tayebati.

Author contributions

S.P., S.V. and Y.S. conceived the original idea and developed the theory, with inputs from C.R.-C. and S.Z.U. M.S. and Y.S. supervised the project. The manuscript was written by S.P. and Y.S. with inputs from all authors.

Competing interests

The authors declare no competing interests.

Additional information

Supplementary information The online version contains supplementary material available at https://doi.org/10.1038/s41467-025-62853-0.

Correspondence and requests for materials should be addressed to Sahil Pontula or Yannick Salamin.

Peer review information *Nature Communications* thanks Chuan-Hua Dong, Fan Wu, and the other anonymous reviewer for their contribution to the peer review of this work. A peer review file is available.